Assimilation of Himawari-8 Rapid-Scan Atmospheric Motion Vectors on Tropical Cyclone in HWRF System

Masahiro Sawada [1],* , **Zaizhong Ma [2]** , **Avichal Mehra [3]** , **Vijay Tallapragada [3]** , **Ryo Oyama [4]** and **Kazuki Shimoji [5]**

[1] Meteorological Research Institute, Japan Meteorological Agency, Tokyo 100-0004, Japan
[2] I. M. Systems Group, Environment Modeling Center, National Centers for Environmental Prediction, NOAA, College Park, MD 20740, USA; zaizhong.ma@noaa.gov
[3] Environment Modeling Center, National Centers for Environmental Prediction, NOAA, College Park, MD 20740, USA; avichal.mehra@noaa.gov (A.M.); vijay.tallapragada@noaa.gov (V.T.)
[4] Asia-Pacific Severe Weather Center, Japan Meteorological Agency, Tokyo 100-0004, Japan; oyama@met.kishou.go.jp
[5] Meteorological Satellite Center, Japan Meteorological Agency, Tokyo 100-0004, Japan; kazuki.shimoji@met.kishou.go.jp
* Correspondence: msawada@mri-jma.go.jp

Abstract: This study investigates the assimilation impact of rapid-scan (RS) atmospheric motion vectors (AMVs) derived from the geostationary satellite Himawari-8 on tropical cyclone (TC) forecasts. Forecast experiments for three TCs in 2016 in the western North Pacific basin are performed using the National Centers for Environmental Prediction (NCEP) operational Hurricane Weather Research and Forecasting Model (HWRF). An ensemble-variational hybrid data assimilation system is used as an initialization. The results show that the assimilation of RS-AMVs can improve the track forecast skill, while the weak bias or slow intensification bias increases at the shorter forecast lead time. A vortex initialization in HWRF has a substantial impact on TC structure, but it has neutral impacts on the track and intensity forecasts. A thinning of AMVs mitigates the weak bias caused by RS-AMV assimilation, resulting in the reduction of intensity error. However, it degrades the track forecast skill for a longer lead time. A decomposition of the TC steering flows demonstrated that the change in TC-induced flow was a primary factor for reducing the track forecast error, and the change in environmental flow has less impact on the track forecast. The investigation of the structural change from the assimilation of RS-AMV revealed that the following two factors are likely related to the intensity forecast degradation: (1) an increase of inertial stability outside the radius of maximum wind (RMW), which weakens the boundary layer inflow; and (2) a drying around and outside the RMW.

Keywords: tropical cyclone; atmospheric motion vector; data assimilation

1. Introduction

The improvement of tropical cyclone (TC) forecast is essential to reduce and mitigate their social and economic impacts. The data assimilation is one of the critical components to improving TC forecast by analyzing the accurate initial condition in previous studies [1–12]. Although the inclusion of the airborne observation in data assimilation has positive impacts on track [13–15], intensity [2,8,12,16,17] and structure [5,8,17,18] of forecasts in the regional models, this data is limited in the western North Pacific. On the other hand, satellite radiance observation or satellite retrieved products such as atmospheric motion vectors (AMVs; [19]), which are derived by tracking clouds or areas of water vapor through consecutive satellite images, are available globally and over the ocean. The AMVs

are important wind information for numerical models around the TC and over the oceans where the conventional wind data is sparse. Therefore, assimilating the frequent and wide coverage AMV data is attractive for the TC forecasts in the operational models.

Rapid-Scan AMV (RS-AMV) consists of the frequent scan of the geostationary satellite with a sub-hourly (5–15 min) time interval. This has a potential to provide the temporally dense observation around the TC. The previous studies remarked that the possibility to improve the TC analysis and forecast by assimilating the RS-AMV [3,4,6,9,11,12]. Himawari-8, the third-generation geostationary meteorological satellite operated by the Japan Meteorological Agency (JMA) in 2015, has achieved significant improvements in resolution, scan frequency, and number of bands [20]. Thus, the Himawari-8 products, such as RS-AMV, are expected to improve TC analysis and forecast through data assimilation. There are some previous studies that investigated the impacts of RS-AMV from Himawari-8. Kunii et al. [21] remarked that the assimilation of RS-AMVs from Himawari-8 into JMA's operational regional model provided better weak and moderate rainfall forecasts, by taking advantage of high-frequency, targeted observation from Himawari-8. Otsuka et al. [22] conducted the data assimilation experiments of RS-AMV for the cold vortex event using the JMA's operational regional model, and it has improved the wind forecasts slightly in early forecast lead times before 12 h. However, the impacts of RS-AMV from Himawari-8 on TC forecast have not been fully investigated.

A vortex initialization (VI) is one of the unique techniques to analyze and initialize the TC vortex in a Hurricane Weather Research and Forecasting (HWRF) model, which is the operational hurricane model at the National Oceanic and Atmospheric Administration (NOAA). VI adjusts vortex structure, intensity, and position based on the observed TC parameters provided by the National Centers for Environmental Prediction (NCEP) TC-Vitals [23,24]. The modification of VI contributed to the reductions in intensity and track forecast errors [25]. However, Tallapragada et al. [26] pointed out the assimilation of the conventional data after performing VI tends to generate larger initial imbalance since the vortex is already close to a balanced state as imposed by VI procedure [24]. To overcome this issue, ensemble-based hybrid assimilation has been implemented in HWRF [8,27]. Lu et al. [27] showed that a continuously cycled hybrid ensemble system in HWRF with the background error covariance created from HWRF ensemble using airborne radar data can produce better TC analysis and forecasts without VI, compared with that created from the Global Ensemble Forecast System. Velden et al. [6] conducted the data assimilation experiments on the RS-AMVs derived from GOES-13 on three TCs over the North Atlantic basin using HWRF. They found that the magnitude of the impact depends on the availability of RS-AMVs and the degree to which unbalanced states are allowed to enter the model analyses through vortex initialization (VI) incorporated in HWRF, though a modest positive impact on track and intensity forecasts can be obtained. Zhang et al. [9] tackled the issue of how the assimilation of high-resolution AMVs with and without VI influences the TC forecast. They revealed that the assimilation of high-resolution AMVs benefits the track and intensity forecast both with and without the VI. Additionally, the assimilation of high-resolution AMVs can alleviate unrealistic vortex modification due to VI, resulting in improved intensity forecasts. Although the impacts of VI on TC forecast over the North Atlantic and eastern North Pacific has been conducted, the investigation over the western North Pacific has not been conducted.

To make efficient use of spatially dense observation data like AMV, data thinning is necessary because, in general, the length of horizontal observation error correlation is shorter than that of RS-AMVs. Several studies documented that the estimated horizontal observation error correlation length for AMVs was 150–200 km [28,29]. Yamashita [30] remarked that the thinning of RS-AMVs from MTSAT-1R had a positive impact on precipitation forecast and showed a slight improvement for the TC intensity forecast. On the other hand, Otsuka et al. [22] showed that data thinning of RS-AMVs had neutral or little positive impacts on the forecast winds and temperatures because more RS-AMVs with a shorter length thinning scale might cause a more positive impact. At least, the degradation originated from spatial observation error correlation between neighboring observations was not be found in their study. Thus, it is worth examining the impact of thinning for RS-AMV on the TC forecast.

This study aims to demonstrate there is the potential to improve TC forecast by assimilating rapid-scan AMVs derived from Himawari-8 for the operational TC forecast model, which is the extension of previous authors' study [11]. Additionally, we investigate impacts of VI by turning off VI and how the RS-AMVs were effectively assimilated by changing the thinning distance of RS-AMVs. This paper is organized as follows. Section 2 describes an overview of RS-AMVs, experimental design of HWRF, and selected TC cases. Section 3 shows statistical verifications of numerical experiments, and axisymmetric structures are examined. Section 4 gives a conclusion of this study.

2. Case and Methodology

2.1. Rapid-Scan Atmospheric Motion Vector of Himawari-8

The Himawari-8 RS-AMVs were computed every 10 min from three consecutive images of the target region taken at 2.5-min intervals for the visible (VIS) channel and at 5-min intervals for the infrared (IR) and Water Vapor (WV) channels. The motion vectors are retrieved from the tracking of the displacements of clouds in forward and backward. The RS-AMVs are derived at approximately 0.02° by 0.02° if the target box is traceable. The height of the motion vectors was assigned based on maximum likelihood estimation with observed radiances from Himawari-8 and the first guess of humidity and temperature profiles from the JMA's global atmospheric model. The algorithm used was the same as the operational AMVs [31]. Error characteristics of RS-AMV were summarized by Otsuka et al. [22], and they showed the root mean square vector differences relative to the sonde observation in the VIS, WV, and IR channels were around 6.4–8.1 m s^{-1} at low-mid levels, 9.1–9.8 m s^{-1} at high-levels.

This study examines the impacts of frequent rapid-scan AMVs in addition to AMVs derived from full-disk imagery. The full-disk scan Himawari-8 AMVs (or operational AMVs) are derived at approximately 0.2° by 0.2° at 30 min intervals if the target box is traceable. We used the operational AMVs (hereafter OPAMV) as a baseline experiment, which describes in next subsection. The observation errors for OPAMV and RS-AMV used in data assimilation system was the same because the algorithm for AMV derivation and its configuration are the same.

2.2. Outline of HWRF and Experimental Design

HWRF is an NCEP operational hurricane forecast system and is a triple-nested, atmosphere–ocean coupled system. HWRF version 3.9 used in this study was obtained from the HWRF developers' repository on 1 March, 2017. The configuration of HWRF is identical to the previous work done by Sawada et al. [11]. The brief description of the configuration is the following. The forecast domain sizes are 80° × 80° with 18-km grid spacing for the parent domain (outermost domain, called d01), 24° × 24° with 6-km grid spacing for the outer nested domain (d02) and is 7° × 7° with 2-km grid spacing for the innermost nested domain (d03). The HWRF has 61 hybrid vertical levels from the surface to 10 hPa. The physical processes include the modified eddy-diffusivity mass-flux planetary boundary layer scheme of NCEP Global Forecast System [32], the scale-aware simplified Arakawa-Schubert convection scheme [33], the Ferrier-Aligo microphysical scheme [34], and the Rapid Radiative Transfer Model for GCMs longwave and shortwave radiation scheme [35]. The details can be found in the HWRF scientific documentation [36].

In HWRF, the atmospheric fields of d01 are initialized from the Global Forecast System analysis, and the first guess for two nested domains (d02 and d03) is a 6-h forecast from the global data assimilation system with VI. The vortex-scale fields originated from the previous 6-h forecast of HWRF when available. The vortex is adjusted based on the TC Vitals and inserted into the first guess. Otherwise, the corrected vortex from the 6-h global data assimilation system forecast is used. After VI, the HWRF Data Assimilation System, which is based on the Gridpoint Statistical Interpolation system, is utilized for the two nested domains (d02 and d03) with a 6-h cycle to generate a vortex structure and its surrounding environment. The assimilation domains (called the ghost d02 and d03) have broader coverage than those of the forecast d02 and d03 and have corresponding domain

sizes of 28° × 28° and 15° × 15°, respectively. For the ensemble-variational hybrid assimilation, the background error covariance of the hybrid system is derived from a mixture of flow-dependent and static sources. The flow-dependent covariance is estimated from the HWRF 40-member ensemble. The static (climatological) covariance is obtained through the National Meteorological Center (now NCEP) method [37,38]. The weighting factor for static and flow-dependent background error covariance is set to 0.2 and 0.8, respectively. The ensemble forecasts of HWRF are initialized or warm-started from the Global Ensemble Forecast System at each cycle in this study.

A merging or blending procedure is applied after data assimilation to combine the HWRF Data Assimilation System analysis to the global data assimilation system analysis to avoid spindown of intense storms [5,8,36]. In the blending procedure, the increments from the HWRF Data Assimilation System analysis are removed below the 600 hPa pressure level if they are within 150 km of the TC center. The increments are gradually reintroduced between 150 and 300 km in the radial direction and between 400 and 600 hPa in the vertical. The blending is used when the maximum sustained wind speed equal to or greater than 65 kt. When the blending is turned on, full or part of increments within 300 km radius and below 400 hPa, which is where the RS-AMV data densely exist, are eliminated. Even though the impact of data assimilation is propagated to the inner core region through the vortex-scale data assimilation cycle during the 6-h forecast, as shown in previous studies [6,10–12], it is worth considering the impact of full increments for the TC inner-core region [9].

To investigate the impacts of RS-AMV on the TC forecast in HWRF, four sets of experiments have been carried out, as shown in Table 1. The initial condition of the CTL (The CTL experiment was identical to the DAhAMV experiment of previous authors' study [11]) experiment is given from the assimilation of conventional and satellite radiances observation data using the ensemble-variational hybrid assimilation method with vortex initialization. The Himawari-8 AMV (OPAMV) was assimilated from three hours prior to one hour after the analysis time. The asymmetric assimilation window was applied to make use of observation data as much as possible within a constraint of cutoff time. In the RAMV experiment, the initial condition was created from the assimilation of observation data used in the CTL experiment and from RS-AMV. The RS-AMV was ingested within one hour of the analysis time. To examine the impacts of vortex initialization on TC forecast and its structure, the RAMV_NVI experiment, which the vortex initialization was turned off, was conducted. By comparing between the RAMV and RAMV_NVI experiments, the effects of vortex initialization are explored. To look into whether the data thinning of RS-AMV has a positive impact on TC forecast by reducing the horizontal observation correlations of dense RS-AMV data, the horizontal thinning distance of 10 km was applied for RS-AMV in the RAMV_T10K experiment. The 10 km thinning distance was applied to the RS-AMVs such that there is only one wind every 10 km by 10 km square. The density of the original RS-AMV is around 20 wind data for 10 km by 10 km square in maximum. The total number of forecast cycles of the three TCs was 73 in each experiment, as shown in Table 2.

Table 1. Outline of control and sensitivity experiments.

Case	Assimilated AMVs	VI	Thinning
CTL	OPAMV	On	None
RAMV	OPAMV + RS-AMV	On	None
RAMV_NVI	OPAMV + RS-AMV	Off	None
RAMV_T10K	OPAMV + RS-AMV	On	10 km

Table 2. List of start and end date of each case used in the experiment.

Case	Cycle Period	No. of Cycles
Nepartak	1800 UTC 2 July–0000 UTC 9 July 2016	26
Meranti	1200 UTC 8 September –1800 UTC 14 September 2016	26
Megi	0600 UTC 23 September –0600 UTC 28 September 2016	21

2.3. Cases of TC

Three TCs over the western North Pacific in 2016 are selected as following Sawada et al. [11]. Figure 1 shows the track and intensity of the three selected TCs: Nepartak, Meranti, and Megi. The track and intensity data were obtained from the Joint Typhoon Warning Center best track. The start and end date when HWRF ran and the number of cycles for each TC are listed in Table 2.
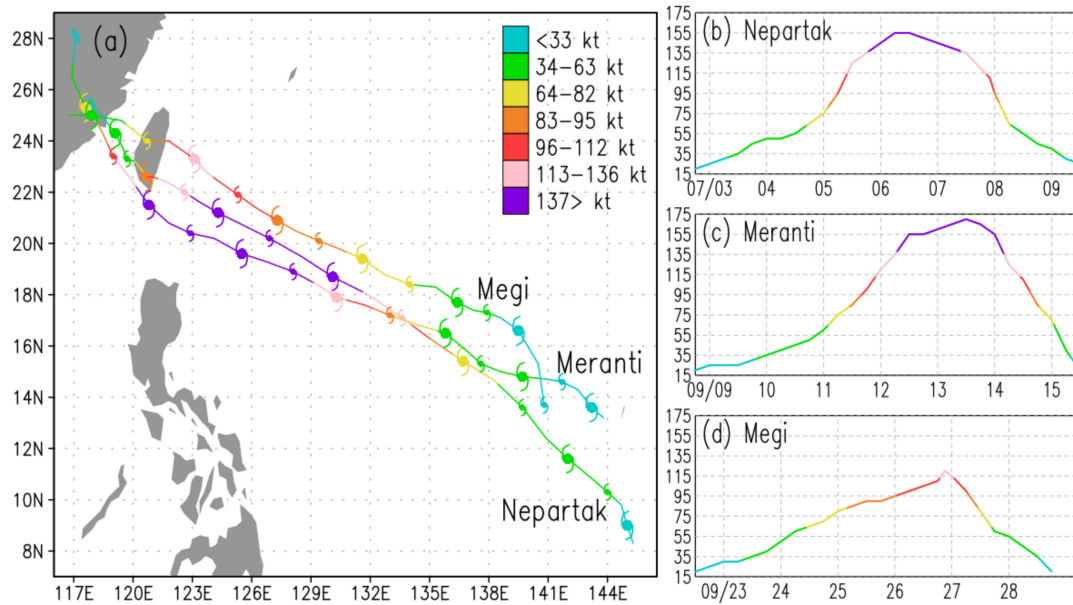

Figure 1. (**a**) TC tracks for Nepartak, Meranti, and Megi. Symbols are plotted with 12-hourly. TC Intensities for (**b**) Nepartak, (**c**) Meranti, and (**d**) Megi. Each line color indicates storm intensity categories on the Saffir-Simpson scale.

3. Results

To evaluate the impacts of RS-AMV, VI, and thinning of AMV data on TC forecast, the verification results of each impact are described, respectively. The skill or improvement rate relative to CTL is defined by

$$SKILL = 100 \, (E_{CTL} - E_{EX})/E_{CTL}, \tag{1}$$

where E_{CTL} and E_{EX} are the mean track error or root-mean-square error (RMSE) of intensity or size from CTL and a given experiment, respectively.

3.1. Track Forecast

The track forecast verification for all three TCs is displayed in Figure 2. The track errors are calculated from the great-circle distance between a cyclone's forecast position and the best track position at the forecast time. The track errors of RAMV and RAMV_NVI is smaller than that of CTL, followed by RAMV_T10K, for whole forecast lead time except at initial time and forecast lead time of 54 h (FT = 54 h). The improvement rates of RAMV and RAMV_NVI with respect to the CTL ranges from 5% to 10% for FT = 6–36 and 60–126 h. This improvement demonstrates that assimilating RS-AMVs benefits the track forecast skill. There is little difference between RAMV and RAMV_NVI, indicating that VI has a neutral impact on track forecast. The track errors of RAMV_T10K increases at the longer lead time (>FT = 48 h) compared to those of RAMV and RAMV_NVI. Applying data thinning to RS-AMVs with a 10 km interval has a negative impact on track forecast in this configuration and the present cases at least. It implies that the positive impact originated from more RS-AMVs with a shorter length thinning scale might outweigh the negative impact originated from spatial observation error correlation between neighboring observations.
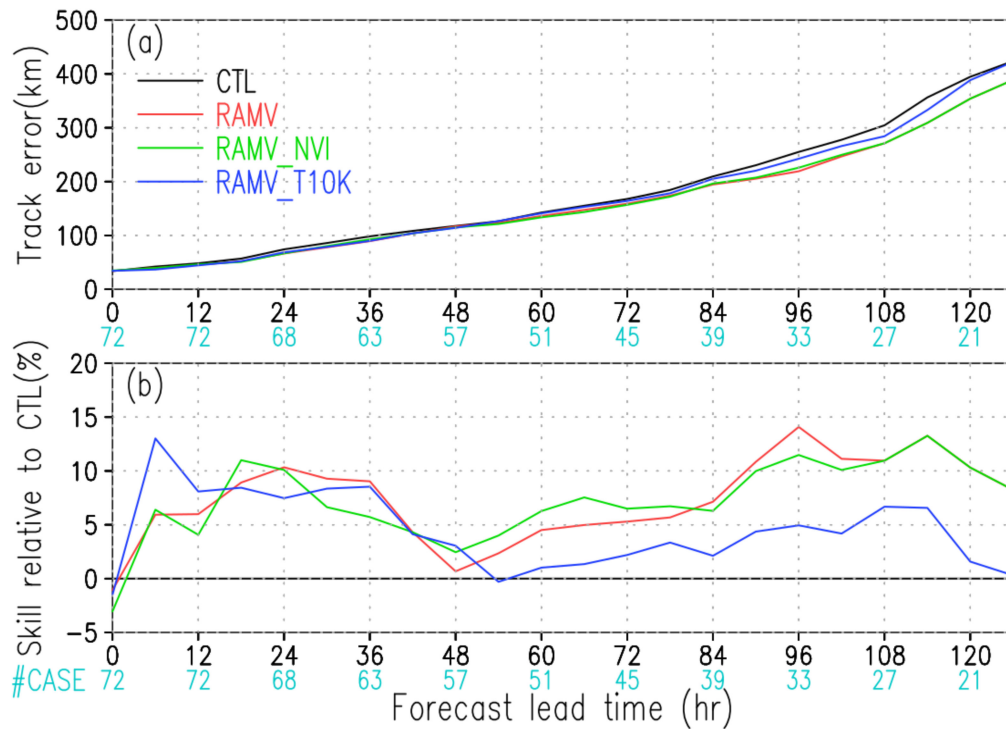
Figure 2. Statistics of (**a**) track error with reference to the best track data and (**b**) track forecast skill relative to CTL for all cases. Numbers in cyan indicate sample size for each forecast lead time.

3.2. Intensity Forecast

The RMSE of maximum sustained surface winds or Vmax showed that RAMV_T10K is the smallest at more than half of forecast lead times in the four experiments (Figure 3). RAMV and RAMV_NVI show the improvement of intensity forecast skill for FT = 6–102 h. The addition of RS-AMV has a positive or neutral impact on intensity forecast except at longer forecast lead times. The RMSE is slightly smaller up to FT = 6–24 in the RAMV_NVI than in the RAMV, but it is slightly larger for FT = 30–48 h. The bias of Vmax shows all the experiments have negative (weak) intensity bias because all the experiments could not reproduce the extremely rapid intensification and its peak intensity for Nepartak and Meranti. The initial weak intensity bias arises from a spindown reported by previous studies [8,11,27]. Sawada et al. [11] remarked that the assimilation with the background error covariance created from the HWRF ensemble effectively alleviates the intensity errors and biases. Even though the Vmax drop at the initial forecast lead time is smaller in this study than in the previous one, it still remains. The biases of Vmax are larger in both RAMV and RAMV_NVI than CTL for the first 12 h, meaning that VI has a little impact on the weak bias at initial forecast time from the viewpoint of the intensity verification. RAMV_T10K shows that the bias is the smallest up to FT = 18 in all the experiments. It indicates there is room to improve the intensity forecast by optimizing the thinning interval.
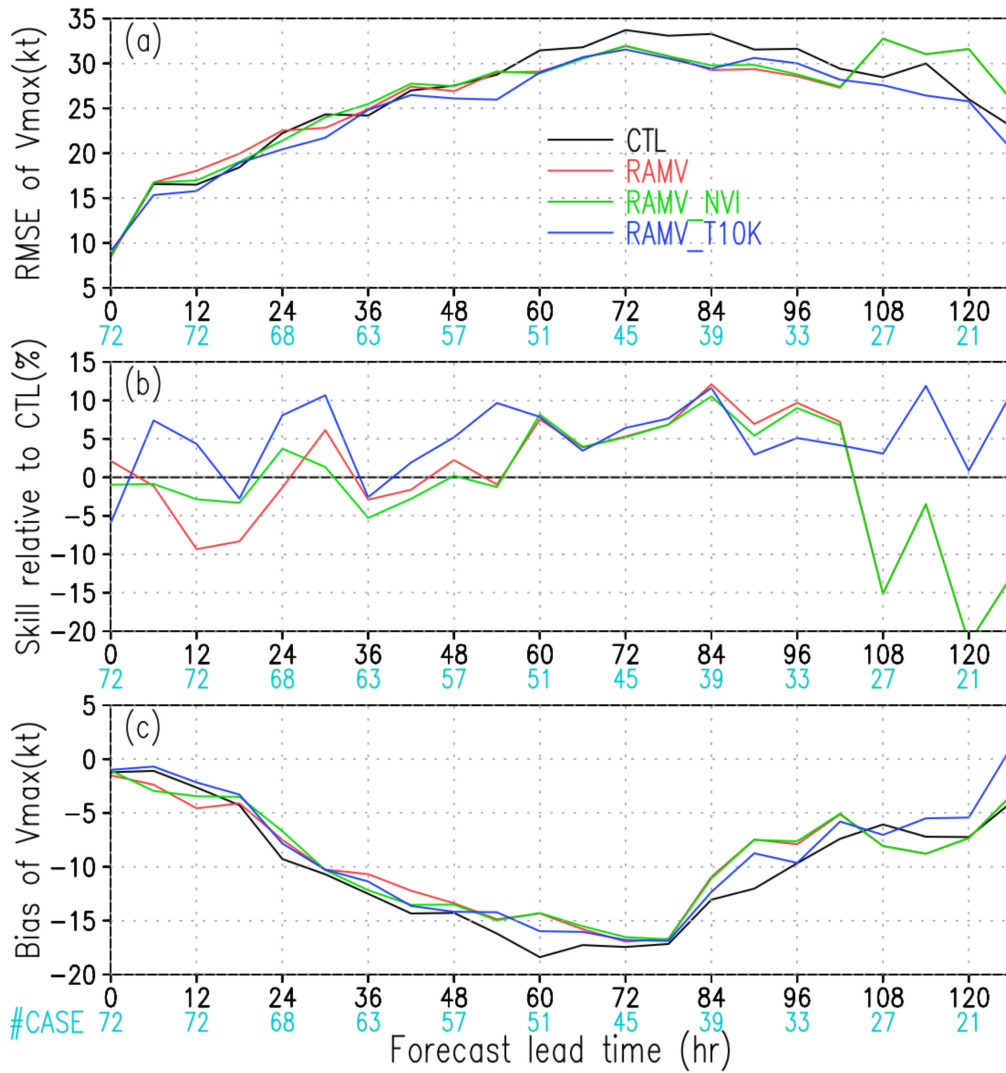
Figure 3. As in Figure 2, but for (**a**) RMSE, (**b**) skill, and (**c**) bias of Vmax.

3.3. Size Forecast

The TC size contains four parameters: the 34-, 50-, and 64-kt wind radii (R34, R50, R64, respectively, hereafter) and radius of maximum wind (RMW). R34, R50, and R64 forecast verification were conducted when averages of the radii over four quadrants were taken. A sample was included in this size verification if at least three of the quadrants have a value for the wind radius and this occurs in all four experiments, to homogenize the sample. RMW forecast was verified for all the cases.

Figure 4 shows the skill of size forecast. Assimilating RS-AMV improves R64 forecast for more than half of forecast lead times, especially up to 36 h. The improvement rates for R64 in RAMV, RAMV_NVI, and RAMV_T10K with respect to CTL reach 13.9%, 13.5%, and 13.4%, respectively, on average for FT = 0–36 h. Compared to CTL, the RMSEs of R50, R64, and RMW tends to decrease for longer forecast lead times, while the RMSE of R34 increases for FT = 114–126 h. The RMW forecast errors became much larger for FT = 0–36 h in RAMV, RAMV_NVI, and RAMV_T10K than in CTL. The assimilation of RS-AMV might deteriorate the representation of TC inner core because the RS-AMVs are too densely distributed around the TC without thinning and/or without accounting for the horizontal observation error covariance. The verification of RMW bias shows that the inclusion of RS-AMV brings about positive (large) bias at early forecast lead times (Figure 5). The positive bias partly contributes to the increase in RMW forecast error. For R34 and R50, amplify the negative (small) bias.
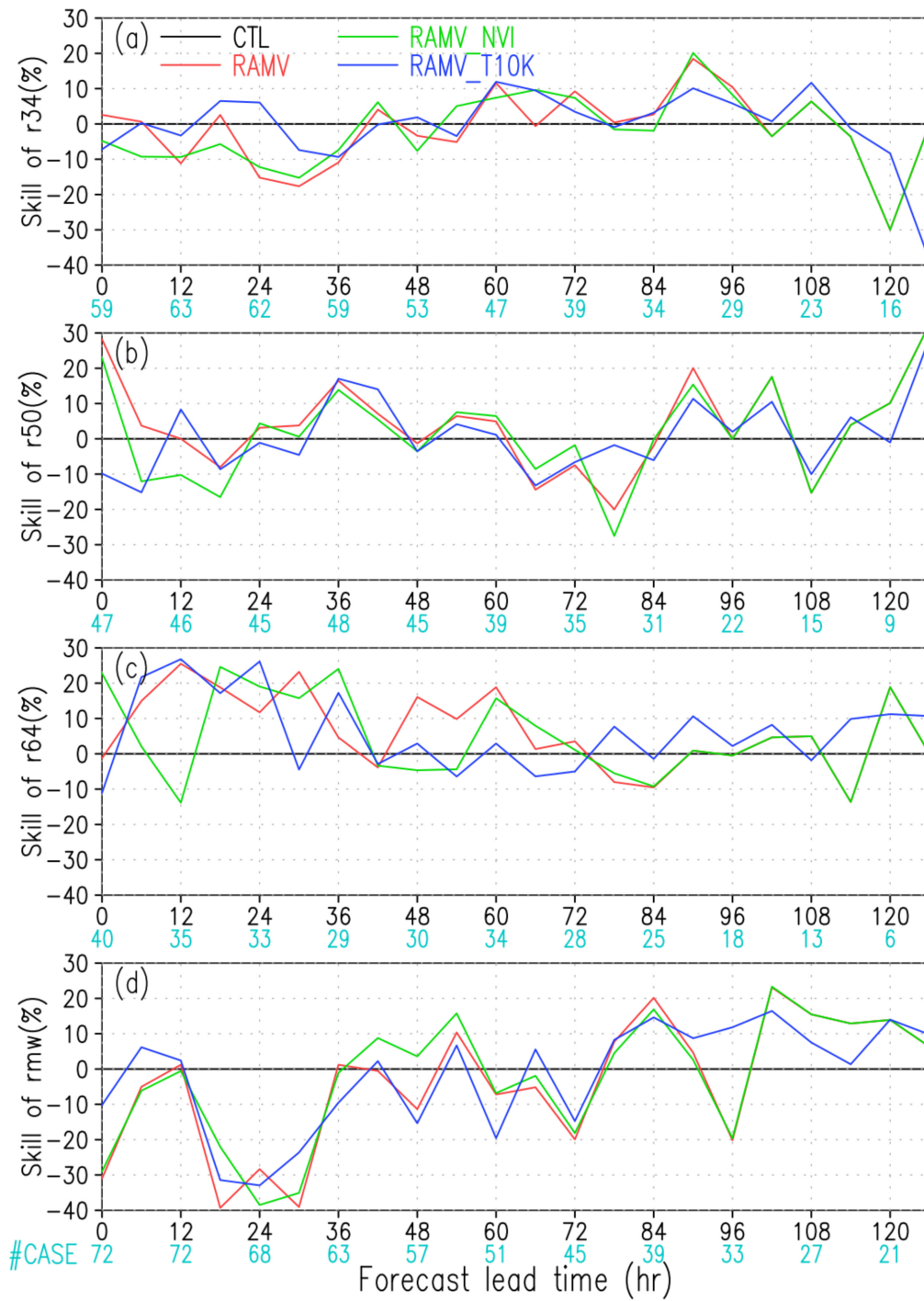
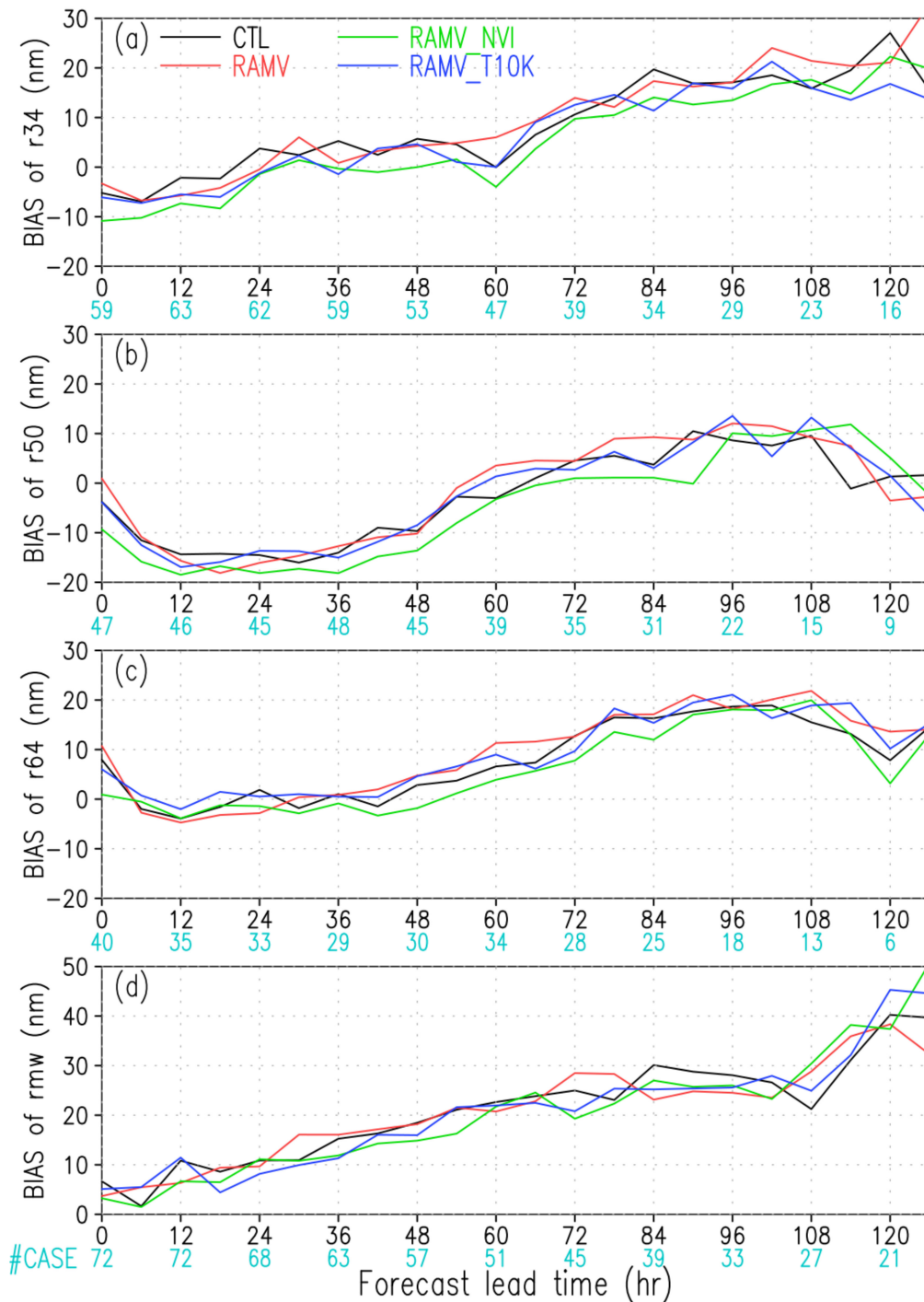**Figure 4.** As in Figure 3, but for skill of (**a**) R34, (**b**) R50, (**c**) R64, and (**d**) RMW.

Figure 5. As in Figure 4, but for bias of (**a**) R34, (**b**) R50, (**c**) R64, and (**d**) RMW.

Surprisingly, VI has positive impacts on R34 and R50 forecast up to 18 h at most, despite that the significant difference in axisymmetric structures can be analyzed at the initial condition, as shown in Section 3.5. The impacts of VI are neutral for R64 and RMW. The negative biases of R50 and R64 in RAMV_NVI are the largest up to FT = 42 and 30 h, respectively, in all the experiments. The negative bias of R34 was larger at early forecast lead times in RAMV_NVI than in RAMV. These suggest that VI has the effect of expanding the TC size, leading to compensation of the negative size biases. Note that the three typhoon cases selected in this study are very intense, and their inner core structures tend to be axisymmetric based on R64 of best track. In that case, VI could help to improve the representation of the inner core vortex structure. Despite that, the improvement seems to be limited in this study.

The initial degradation of R34 and RMW forecast by assimilating RS-AMV was slightly alleviated in RAMV_T10K, implying that the thinning method and/or horizontal observation error covariance needs to be optimized to make more effective use of dense RS-AMVs. There is little difference in biases for all metrics between RAMV and RAMV_T10K.

Overall, the impacts of RS-AMV assimilation on TC sizes is not coherent because the impacts are mixed among the metrics and the forecast lead times. However, it is clear that the biases of R34 and RMW increase with the forecast lead time in all the experiments, which is consistent with Sawada et al. [11]. The increasing trend of TC size bias can also be found for TCs over the North Atlantic by Lim et al. [10]. These results imply the systematic bias of TC size originates from the physical schemes in HWRF, not the initial condition. Even though the vortex initialization has remarkable impacts on axisymmetric TC structures, there were little differences in R34 and RMW in the viewpoint of verification.

3.4. Track Error Analysis

As shown in Figure 2, the improvement in track forecast skill by assimilating high-resolution AMVs is roughly consistent with previous studies [6,11,12]. Sawada et al. [11] and Li et al. [12] remarked that the assimilation of AMVs had a positive impact on track at the longer-range lead time, though Velden et al. [6] showed that the inclusion of the enhanced AMVs had a benefit to track forecast at shorter range lead times. The substantial reduction of track error at the longer-range lead time is interesting because the RS-AMV data used in this study were distributed within around 1000 km square from the TC center, which could not change the broader scale environmental steering flow. Sawada et al. [11] attempted to explain the factor of track error reduction based on the optimum steering flow diagnosis proposed by Galarneau and Davis [39]. The diagnosis indicated the small initial steering flow differences seem to contribute to putting TCs on different trajectories, which is nearer to the actual one. To examine the forecasted track difference, the difference between CTL and RAMV for Nepartak is analyzed because the difference between the two was the largest.

Figure 6 shows an example of circulation patterns decomposed into two components: environmental flows and TC-induced flows based on optimal steering flow diagnosis [39]. Simulated flows were 48 forecast hours for Nepartak initialized at 1200 UTC 4 July 2016. The optimal steering radius and depth were 300 km and 400 hPa from 850 to 450 hPa on average, respectively, from the diagnosis of Sawada et al. [11]. Thus, the steering flows were calculated by averaging within the radius of 300 km from the TC center and between 850 and 450 hPa in vertical. It is evident from Figure 6a that the environmental flows for CTL and RAMV overlapped each other. From Figure 6c, which indicates the difference between CTL and RAMV (RAMV minus CTL), there were small differences in environmental flows (1 ms^{-1} at most) around the TC and little differences (less than 0.5 ms^{-1}) outside the 1000 km from the TC center. The slight difference in environmental flows indicates the assimilation of RAMV does not change the environmental flows even for longer forecast lead time. The difference in TC-induced flows between CTL and RAMV was found around the TC in Figure 6b,c. The vector differences in TC-induced flows display stronger east-northeasterly component in RAMV than in CTL, leading to the westward movement of the forecasted TC in RAMV. The TC-induced flow difference seems to be similar to the flow pattern induced by the beta gyre effect. However, the weaker tangential flow in RAMV would not enhance the beta gyre. The alternative interpretation is that the assimilation of RAMV has imposed a wavenumber-1 flow to the vortex, and the flow difference might be amplified with forecast lead time. The flow pattern differences may explain the reduction of track forecast by assimilating that RAMV comes from the TC-induced flows, not the environmental flows.
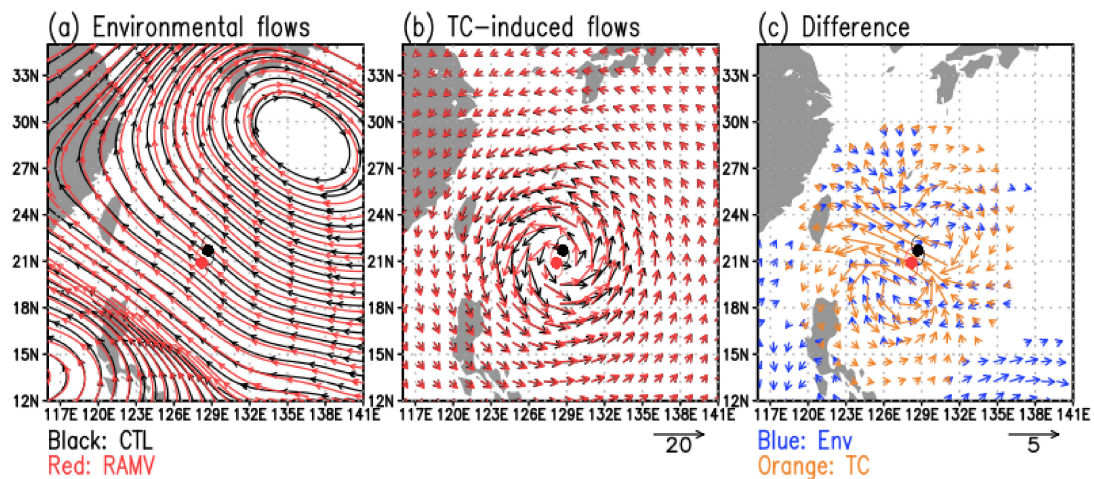
Figure 6. Circulation patterns separated into (**a**) environmental flows, and (**b**) TC-induced flows at 48 forecast hours for Nepartak initialized 1200 UTC 4 July 2016, in CTL (Black) and RAMV (Red). (**c**) Difference in environmental flows with blue vectors and TC-induced flows with orange vectors between RAMV and CTL (RAMV minus CTL). Vector differences smaller than 0.5 m s^{-1} are omitted for clarity. TC Symbols display TC position for CTL (Black) and RAMV (Red).

However, the TC-induced flow difference or beta gyre flow pattern seems to be caused by the difference of TC position between CTL and RAMV. To further evaluate the factor of track difference, TC movements are calculated, in the same manner as forward trajectory, from the steering flow that is a combination of the environmental and TC-induced flows. As a premise, the TC movement is well represented by the forward trajectory calculation using the steering flow combination. To confirm the premise, the TC movements were calculated using the sum of environmental and TC-induced flows by CTL (SF_envCTL_tcCTL) and by RAMV (SF_envRAMV_tcRAMV), respectively. In Figure 7, both SF_envCTL_tcCTL and SF_envRAMV_tcRAMV matched with the forecasted track by CTL (FTRK_CTL) and RAMV (FTRK_RAMV). The result shows the TC movement calculation using the steering flow combination can represent the forecasted track reasonably, and it will be possible to decompose the impact of steering flows on the TC track.

Additional TC trajectories were calculated to investigate which is the key factor to the track error reduction—the environmental flow or TC-induced flow. If the TC-induced flows contribute to the reduction of the track error, the sum of the environmental flow by CTL and the TC-induced flow by RAMV (SF_envCTL_tcRAMV) could be obtained the better TC trajectory than the sum of the environmental flow by RMAV and the TC-induced flow by CTL (SF_envRAMV_tcCTL). Figure 7 demonstrated that SF_envCTL_tcRAMV and SF_envRAMV_tcCTL overlap FTRK_RAMV (SF_envRAMV_tcRAMV) and FTRK_CTL (SF_envCTL_tcCTL), respectively. It is evident that the TC-induced flow plays a primary role in reducing the track error, and the impact of environmental flow is negligible in this case. Note that there is nonlinear interaction between the environmental flow and the TC-induced flow, and it has the potential to affect the TC track, which would amplify with forecast lead time. It is difficult to evaluate the nonlinear interaction effect in this simple framework and beyond the scope of this study.
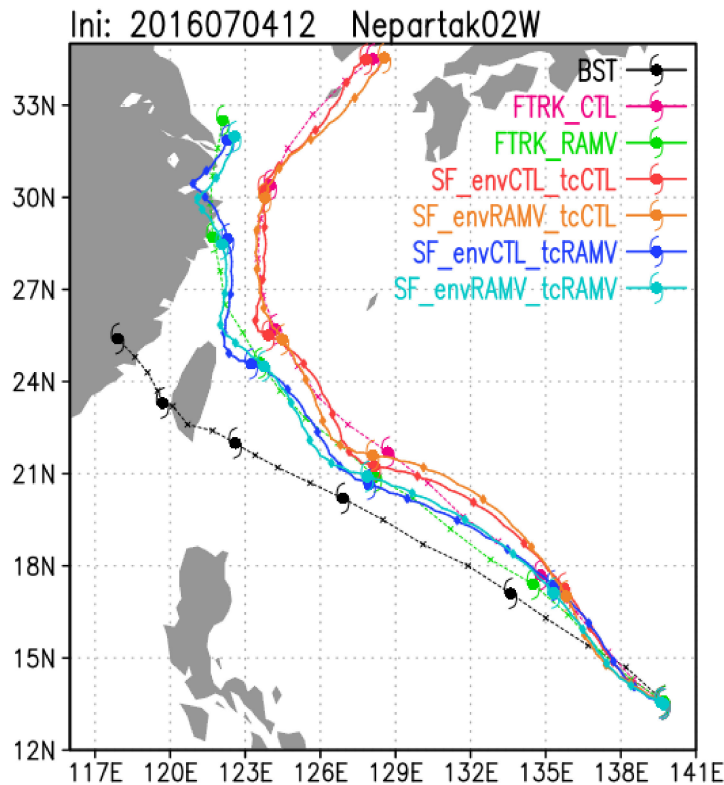
Figure 7. Forecasted track for Nepartak initialized at 1200 UTC 4 July 2016. BST is the best track. FTRK_CTL and FTRK_RAMV are the forecasted track by CTL and RAMV. SF indicates the trajectory calculated from the steering flows. envCTL and envRAMV represent the environmental flows by CTL and RAMV, respectively. tcCTL and tcRAMV represent the TC-induced flows by CTL and RAMV, respectively. TC symbols are plotted with a 24-h interval.

3.5. Axisymmetric Structures

The axisymmetric components were examined how the initial condition affect the TC intensification. To compare the simulated results in this study with the previous observational studies [40,41], the HWRF output on pressure coordinates was interpolated to the height coordinate. The radial structure is normalized by the radius of maximum azimuthally averaged wind at a 2-km altitude based on a previous study [40] to highlight the difference in essential TC structure. The composite is produced by averaging 18 cycles from cycle 3 to cycle 20, corresponding to Meranti's intensification through to the mature stage. The averaged RMWs at a 2-km altitude were 63.8, 69.0, 71.8, and 64.1 km in CTL, RAMV, RAMV_NVI, and RAMV_T10K, respectively.

The azimuthally averaged tangential wind speeds at the initial (FT = 0) are compared in Figure 8. The assimilation of RS-AMV weakens the axisymmetric component of vortices outside the RMW at the upper troposphere. The azimuthally averaged tangential wind speed of RAMV_NVI was the smallest in the four experiments, followed by RAMV, and by RMAV_T10K. Without VI, the TC vortex was weakened from the lower throughout to the upper atmosphere, and it was a raw impact of RS-AMV assimilation on the TC structure. VI makes the TC vortex stronger, and the axis of RMW tilts outward. By thinning the RS-AMV data, the weakening of the tangential wind was alleviated because the excessive increment by RS-AMV was reduced.

Figure 9 shows the radial wind differences averaged for FT = 0–12 h between each experiment and CTL for the lower troposphere. Note that negative values in contour indicate the radial inflows and red color areas are positive anomalies from CTL, meaning that the weakening of radial inflows to CTL. The low-level inflows were weaker in RAMV and RAMV_NVI than CTL and RAMV_T10K, indicating that the RS-AMV assimilation weakens the low-level inflow. The maximum low-level inflow

speeds are 12.4, 10.9, 10.1, and 11.9 m s^{-1} in CTL, RAMV, RAMV_NVI, and RAMV_T10K, respectively. The weakening of low-level inflow was alleviated by thinning the RS-AMV data.

The moisture in the inner core (within a 300-km radius from the TC center) has a significant impact on the TC intensification [42]. To examine the difference in inner core moisture distribution, the azimuthally averaged relative humidity at the initial (FT = 0) is compared in Figure 10. Assimilating RS-AMV makes the initial vortices moisten within the RMW above a 5-km height and dry lower troposphere and outside the RMW. The response in the inner core is consistent with the pattern of initial vortices as shown in Figure 8, which means the stronger vortices are, the drier the vortices become in the inner core. The background error covariance generated from the HWRF ensemble provides cross-variable correlations in the TC inner core reasonably. The drying around and outside the RMW will slow the intensification, implying that the weak bias partly arises from the drying tendency caused by RS-AMV assimilation. Without VI, the inner core became drier because the TC vortex became weak compared to RAMV. Compared to RAMV, the thinning of RS-AMV mitigates the drying outside the RMW so that weak bias caused by RS-AMV assimilation will be alleviated.
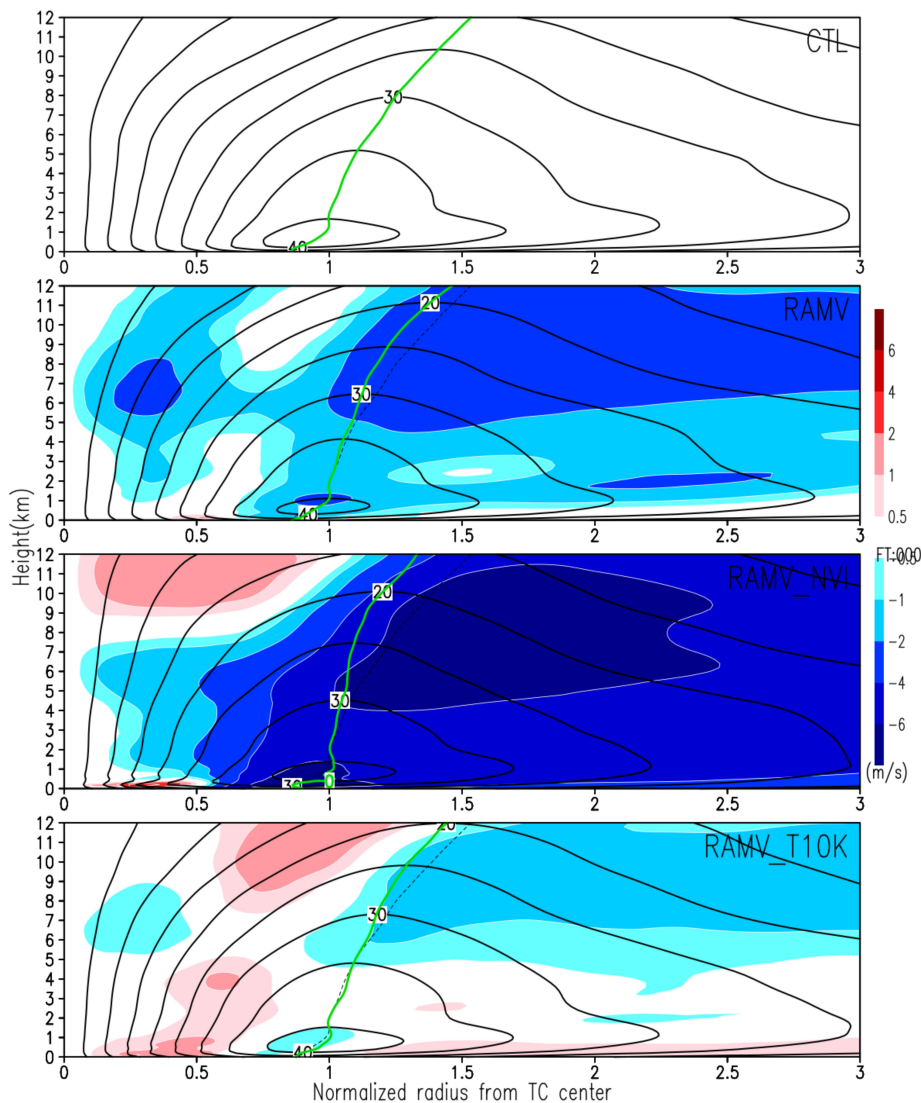

Figure 8. Radial-height cross section of azimuthally averaged tangential wind (contour) at the initial (FT = 0) for Meranti. Color shading display the difference in azimuthally averaged wind (each experiment minus CTL). Green and black dashed lines indicate the radius of maximum wind (RMW) at each height for each experiment and CTL, respectively.
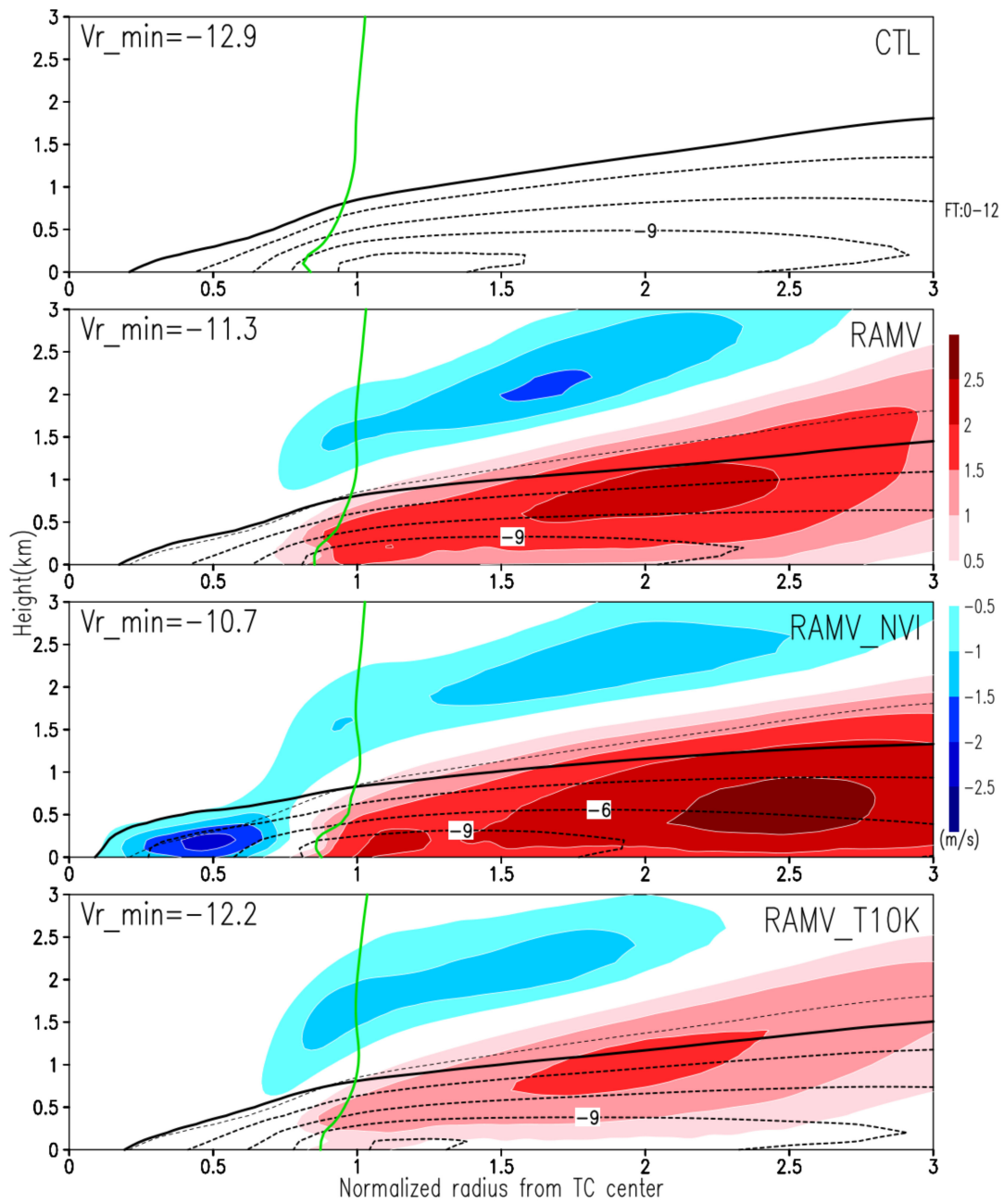
Figure 9. As in Figure 8, but for radial wind azimuthally and temporally averaged for FT = 0–12 h. Note that negative values in contour indicate the radial inflows and red color areas are positive anomalies from CTL, meaning that the weakening of radial inflows to CTL.
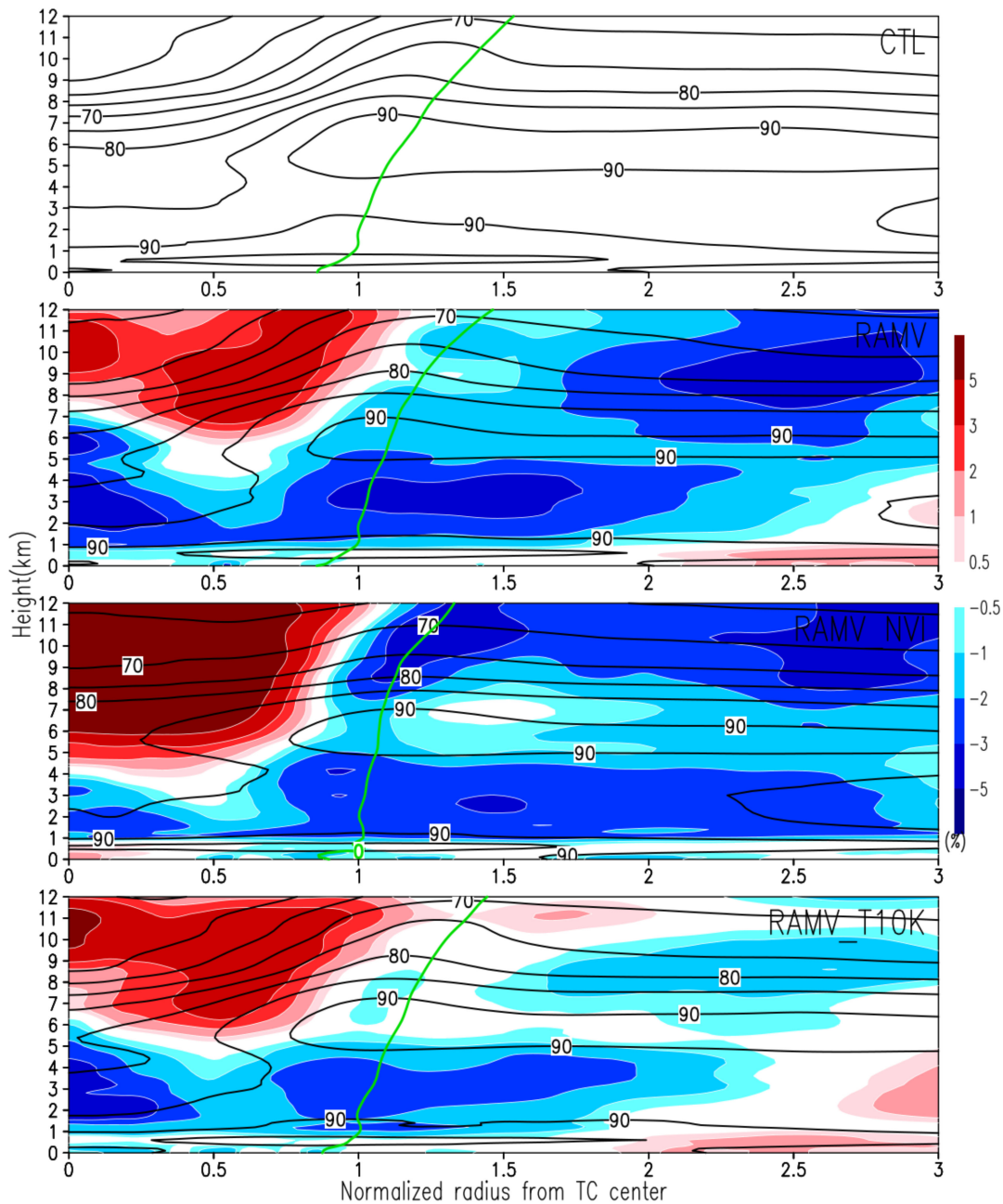
Figure 10. As in Figure 8, but for relative humidity.

4. Conclusions

To extend our previous research work about the TC forecast improvements through assimilating the high-spatiotemporal Himawari-8 AMVs, we investigated how RS-AMV assimilation has impacts on TC track, intensity, and size forecasts with the operational HWRF system in this paper. RS-AMV data provided around 1000 km square at TC center and with a 10-min interval. This is much denser than the AMV data used in the previous study. Target cases of this study are three TCs over the western North Pacific in 2016. RS-AMV data are assimilated using ensemble-variational hybrid data assimilation.

Results from the inclusion of RS-AMV show improvements in the track forecast. The improvement rate with regard to the CTL is 10 % larger at shorter and longer forecast lead times (FT = 6–24, 84–126 h). The intensity forecast error was reduced at longer forecast lead times by assimilating RS-AMV, although the weak bias increases slightly at the initial forecast lead time (FT = 6–12 h).

The R64 forecast was also improved at the shorter forecast lead times by assimilating RS-AMV, while RMW was substantially degraded.

A comparison between the experiments with and without VI shows that there is little difference in track and intensity forecast skills in the statistical verification, while the axisymmetric structures have remarkable differences between the two. VI could help to improve the representation of the inner core vortex structure when the typhoon is intense and has an axisymmetric structure such as the selected typhoons in this study. However, the impact of VI was limited. The limited impacts of VI imply that the dense AMV (RS-AMV) assimilation has the potential to provide the axisymmetric component of TCs, which lead to intensification of TC, instead of using VI. Furthermore, it might be one of the options to shift from the VI with craftsmanship to the sophisticated objective analysis method combined with dense satellite observations surrounding TC such as microwave sounding like TROPICS [43], GPS-based observation like CYGNSS [44], geostationary microwave sounder [45] and L-band wind speed from Soil Moisture Ocean Salinity mission [46] and Soil Moisture Active Passive mission [47]. These dense observational systems will capture the asymmetric component of TC, which cannot be obtained from the VI [48].

To examine the impact of horizontal observation error correlations of RS-AMVs, the AMV horizontal thinning distance of 10 km was conducted. The thinning of AMV data has substantial impacts on track and intensity forecast. By applying the thinning to the AMV data, the track forecast skill was improved only for the first 12 h but was degraded beyond FT = 60 h compared to the experiment without thinning. On the other hand, the experiment with thinning shows the intensity forecast skill was improved at more than half of forecast lead times. These indicate that the current thinning process and/or assimilation configuration is suboptimal for the track forecast. The horizontal observation error correlations of RS-AMVs is nonnegligible because the RS-AMVs used in this study were densely derived. One of the possible ways to solve this issue without adjusting the thinning distance is to treat the off-diagonal component of the observation error covariance matrix. An additional experiment with a configuration using RS-AMVs and where VI is off but thinning is on may help to understand the impact of thinning because the VI has a considerable influence on the TC inner core structure, which may hinder the thinning impact.

As further use of satellite data products, the rapid data assimilation cycle, such as 5–15-min intervals, has the potential to improve the TC analysis and forecast [49] and TC-induced rainfall forecast [21,49], and isolated convective rainfall [48]. Incorporating these sophisticated assimilation systems is beyond the scope of this study but is a worthwhile direction for future research. The direct radiance assimilation is another straightforward way to make use of the satellite observation [49–52], which will complement each other as information different from AMV.

Author Contributions: Conceptualization, M.S., Z.M. and R.O.; methodology, M.S. and Z.M.; software, Z.M. and K.S.; validation, M.S.; formal analysis, M.S.; resources, M.S.; data curation, K.S. and R.O.; writing—original draft preparation, M.S.; writing—Review and editing, M.S.; visualization, M.S.; supervision, A.M.; project administration, A.M. and V.T.; funding acquisition, M.S., A.M. and V.T. All authors have read and agreed to the published version of the manuscript.

Conflicts of Interest: The authors declare no conflict of interest.

References

1. Aberson, S.D.; Franklin, J.L. Impact on hurricane track and intensity forecasts of GPS dropwindsonde observations from the first-season flights of the NOAA Gulfstream-IV Jet Aircraft. *Bull. Am. Meteorol. Soc.* **1999**, *80*, 421–427. [CrossRef]
2. Aberson, S.; Aksoy, D.A.; Sellwood, K.J.; Vukicevic, T.; Zhang, X. Assimilation of high-resolution tropical cyclone observations with an ensemble Kalman filter using HEDAS: Evaluation of 2008–11 HWRF forecasts. *Mon. Weather Rev.* **2015**, *143*, 511–523. [CrossRef]
3. Wu, T.; Liu, H.; Majumdar, S.J.; Velden, C.S.; Anderson, J.L. Influence of Assimilating Satellite-Derived Atmospheric Motion Vector Observations on Numerical Analyses and Forecasts of Tropical Cyclone Track and Intensity. *Mon. Weather Rev.* **2014**, *142*, 49–71. [CrossRef]
4. Wu, T.; Velden, C.S.; Majumdar, S.J.; Liu, H.; Anderson, J.L. Understanding the Influence of Assimilating Subsets of Enhanced Atmospheric Motion Vectors on Numerical Analyses and Forecasts of Tropical Cyclone Track and Intensity with an Ensemble Kalman Filter. *Mon. Weather Rev.* **2015**, *143*, 2506–2531. [CrossRef]
5. Pu, Z.; Zhang, S.; Tong, M.; Tallapragada, V. Influence of the Self-Consistent Regional Ensemble Background Error Covariance on Hurricane Inner-Core Data Assimilation with the GSI-Based Hybrid System for HWRF. *J. Atmos. Sci.* **2016**, *73*, 4911–4925. [CrossRef]
6. Velden, C.; Lewis, W.E.; Bresky, W.; Stettner, D.; Daniels, J.; Wanzong, S. Assimilation of High-Resolution Satellite-Derived Atmospheric Motion Vectors: Impact on HWRF Forecasts of Tropical Cyclone Track and Intensity. *Mon. Weather Rev.* **2017**, *145*, 1107–1125. [CrossRef]
7. Elsberry, R.L.; Hendricks, E.A.; Velden, C.S.; Bell, M.M.; Peng, M.; Casas, E.; Zhao, Q. Demonstration with Special TCI-15 Datasets of Potential Impacts of New-Generation Satellite Atmospheric Motion Vectors on Navy Regional and Global Models. *Weather Forecast.* **2018**, *33*, 1617–1637. [CrossRef]
8. Tong, M.; Sippel, J.A.; Tallapragada, V.; Liu, E.; Kieu, C.; Kwon, I.; Wang, W.; Liu, Q.; Ling, Y.; Zhang, B. Impact of Assimilating Aircraft Reconnaissance Observations on Tropical Cyclone Initialization and Prediction Using Operational HWRF and GSI Ensemble-Variational Hybrid Data Assimilation. *Mon. Weather Rev.* **2018**, *146*, 4155–4177. [CrossRef]
9. Zhang, S.; Pu, Z.; Velden, C. Impact of Enhanced Atmospheric Motion Vectors on HWRF Hurricane Analyses and Forecasts with Different Data Assimilation Configurations. *Mon. Weather Rev.* **2018**, *146*, 1549–1569. [CrossRef]
10. Lim, A.H.N.; Jung, J.A.; Nebuda, S.E.; Daniels, J.M.; Bresky, W.; Tong, M.; Tallapragada, V. Tropical Cyclone Forecasts Impact Assessment from the Assimilation of Hourly Visible, Shortwave, and Clear-Air Water Vapor Atmospheric Motion Vectors in HWRF. *Weather Forecast.* **2019**, *34*, 177–198. [CrossRef]
11. Sawada, M.; Ma, Z.; Mehra, A.; Tallapragada, V.; Oyama, R.; Shimoji, K. Impacts of Assimilating High-Resolution Atmospheric Motion Vectors Derived from Himawari-8 on Tropical Cyclone Forecast in HWRF. *Mon. Weather Rev.* **2019**, *147*, 3721–3740. [CrossRef]
12. Li, J.; Li, J.; Velden, C.; Wang, P.; Schmit, T.J.; Sippel, J. Impact of rapid-scan-based dynamical information from GOES-16 on HWRF hurricane forecasts. *J. Geophys. Res. Atmos.* **2020**, *125*. [CrossRef]
13. Chan, P.; Wu, N.; Zhang, C.; Deng, W.; Hon, K. The first complete dropsonde observation of a tropical cyclone over the South China Sea by the Hong Kong Observatory. *Weather* **2018**, *73*, 227–234. [CrossRef]
14. Ito, K.; Yamada, H.; Yamaguchi, M.; Nakazawa, T.; Nagahama, N.; Shimizu, K.; Ohigashi, T.; Shinoda, T.; Tsuboki, K. Analysis and forecast using dropsonde data from the inner-core region of Tropical Cyclone Lan (2017) obtained during the first aircraft missions of T-PARCII. *SOLA* **2018**, *14*, 105–110. [CrossRef]
15. Gao, Y.; Xiao, H.; Jiang, D.; Wan, Q.; Chan, P.W.; Hon, K.K.; Deng, G. Impacts of Thinning Aircraft Observations on Data Assimilation and Its Prediction during Typhoon Nida (2016). *Atmosphere* **2019**, *10*, 754. [CrossRef]
16. Torn, R.D. The Impact of Targeted Dropwindsonde Observations on Tropical Cyclone Intensity Forecasts of Four Weak Systems during PREDICT. *Mon. Weather Rev.* **2014**, *142*, 2860–2878. [CrossRef]
17. Feng, J.; Wang, X. Impact of Assimilating Upper-Level Dropsonde Observations Collected during the TCI Field Campaign on the Prediction of Intensity and Structure of Hurricane Patricia (2015). *Mon. Weather Rev.* **2019**, *147*, 3069–3089. [CrossRef]

18. Christophersen, H.; Aksoy, A.; Dunion, J.; Sellwood, K.J. The impact of NASA Global Hawk unmanned aircraft dropwindsonde observations on tropical cyclone track, intensity, and structure: Case studies. *Mon. Weather Rev.* **2017**, *145*, 1817–1830. [CrossRef]

19. Velden, C.; Daniels, J.; Stettner, D.; Santek, D.; Key, J.; Dunion, J.; Holmlund, K.; Dengel, G.; Bresky, W.; Menzel, P. Recent Innovations in Deriving Tropospheric Winds from Meteorological Satellites. *Bull. Am. Meteorol. Soc.* **2005**, *86*, 205–224. [CrossRef]

20. Bessho, K.; Date, K.; Hayashi, M.; Ikeda, A.; Imai, T.; Inoue, H.; Kumagai, Y.; Miyakawa, T.; Murata, H.; Ohno, T.; et al. An introduction to Himawari-8/9—Japan's new-generation geostationary meteorological satellites. *J. Meteorol. Soc. Jpn.* **2016**, *94*, 151–183. [CrossRef]

21. Kunii, M.; Otsuka, M.; Shimoji, K.; Seko, H. Ensemble data assimilation and forecast experiments for the September 2015 heavy rainfall event in Kanto and Tohoku regions with atmospheric motion vectors from Himawari-8. *SOLA* **2016**, *12*, 209–214. [CrossRef]

22. Otsuka, M.; Seko, H.; Shimoji, K.; Yamashita, K. Characteristics of Himawari-8 rapid scan atmospheric motion vectors utilized in mesoscale data assimilation. *J. Meteorol. Soc. Jpn.* **2018**, *96B*, 111–131. [CrossRef]

23. Liu, Q.; Surgi, N.; Lord, S.; Wu, W.-S.; Parrish, S.; Gopalakrishnan, S.; Waldrop, J.; Gamache, J. Hurricane initialization in HWRF model. In Proceedings of the 27th Conference on Hurricanes and Tropical Meteorology, Monterey, CA, USA, 23–28 April 2006. Available online: http://ams.confex.com/ams/pdfpapers/108496.pdf (accessed on 20 April 2020).

24. Liu, Q.; Zhang, X.; Trahan, S.; Tallapragada, V. Extending operational HWRF initialization to triple-nest HWRF system. In Proceedings of the 30th Conference on Hurricanes and Tropical Meteorology, Ponte Vedra Beach, FL, USA, 15–20 April 2012. Available online: https://ams.confex.com/ams/30Hurricane/webprogram/Paper204853.html (accessed on 20 April 2020).

25. Goldenberg, S.B.; Gopalakrishnan, S.G.; Tallapragada, V.; Quirino, T.; Marks, F.; Trahan, S.; Zhang, X.; Atlas, R. The 2012 Triply Nested, High-Resolution Operational Version of the Hurricane Weather Research and Forecasting Model (HWRF): Track and Intensity Forecast Verifications. *Weather Forecast.* **2015**, *30*, 710–729. [CrossRef]

26. Tallapragada, V.; Kieu, C.; Kwon, Y.; Trahan, S.; Liu, Q.; Zhang, Z.; Kwon, I.-H. Evaluation of storm structure from the operational HWRF Model during 2012 implementation. *Mon. Weather Rev.* **2014**, *142*, 4308–4325. [CrossRef]

27. Lu, X.; Wang, X.; Li, Y.; Tong, M.; Ma, X. GSI-based ensemble-variational hybrid data assimilation for HWRF for hurricane initialization and prediction: Impact of various error covariances for airborne radar observation assimilation. *Q. J. R. Meteorol. Soc.* **2017**, *143*, 223–239. [CrossRef]

28. Otsuka, M.; Kunii, M.; Seko, H.; Shimoji, K.; Hayashi, M.; Yamashita, K. Assimilation experiments of MTSAT rapid scan atmospheric motion vectors on a heavy rainfall event. *J. Meteorol. Soc. Jpn.* **2015**, *93*, 459–475. [CrossRef]

29. Cordoba, M.; Dance, S.L.; Kelly, G.A.; Nichols, N.K.; Waller, J.A. Diagnosing atmospheric motion vector observation errors for an operational high-resolution data assimilation system. *Q. J. R. Meteorol. Soc.* **2017**, *143*, 333–341. [CrossRef]

30. Yamashita, K. An observing system experiment of MTSAT-2 rapid scan AMV using JMA meso-scale operational NWP system. In Proceedings of the 11th International Winds Workshop, Auckland, New Zealand, 20–24 February 2012. Available online: http://cimss.ssec.wisc.edu/iwwg/iww11/talks/Session4_Yamashita2.pdf (accessed on 20 April 2020).

31. Shimoji, K. Motion Tracking and Cloud Height Assignment Methods for Himawari-8 AMV. In Proceedings of the 12th International Winds Workshop, Copenhagen, Denmark, 16–20 June 2014. Available online: http://cimss.ssec.wisc.edu/iwwg/iww12/talks/01_Monday/1710_IWWG_0616_2_algorithm_Shimoji_final.pdf (accessed on 20 April 2020).

32. Han, J.; Witek, M.; Teixeira, J.; Sun, R.; Pan, H.-L.; Fletcher, J.K.; Bretherton, C.S. Implementation in the NCEP GFS of a Hybrid Eddy-Diffusivity Mass-Flux (EDMF) boundary layer parameterization with dissipative heating and modified stable boundary layer mixing. *Weather Forecast.* **2016**, *31*, 341–352. [CrossRef]

33. Han, J.; Wang, W.; Kwon, Y.C.; Hong, S.; Tallapragada, V.; Yang, F. Updates in the NCEP GFS cumulus convection schemes with scale and aerosol awareness. *Weather Forecast.* **2017**, *32*, 2005–2017. [CrossRef]

34. Aligo, E.A.; Ferrier, B.; Carley, J.R. Modified NAM Microphysics for Forecasts of Deep Convective Storms. *Mon. Weather Rev.* **2018**, *146*, 4115–4153. [CrossRef]

35. Iacono, M.J.; Delamere, J.S.; Mlawer, E.J.; Shephard, M.W.; Clough, S.A.; Collins, W.D. Radiative forcing by long-lived greenhouse gases: Calculations with the AER radiative transfer models. *J. Geophys. Res.* **2008**, *113*, D13103. [CrossRef]

36. Biswas, M.K.; Abarca, S.; Bernardet, L.; Ginis, I.; Grell, E.; Iacono, M.; Kalina, E.; Liu, B.; Liu, Q.; Marchok, T.; et al. Hurricane Weather Research and Forecasting (HWRF) Model: 2018 Scientific Documentation. Available online: https://dtcenter.org/HurrWRF/users/docs/index.php (accessed on 20 April 2020).

37. Parrish, D.F.; Derber, J.C. The National Meteorological Center's Spectral Statistical-Interpolation Analysis System. *Mon. Weather Rev.* **1992**, *120*, 1747–1763. [CrossRef]

38. Wu, W.; Purser, R.J.; Parrish, D.F. Three-Dimensional Variational Analysis with Spatially Inhomogeneous Covariances. *Mon. Weather Rev.* **2002**, *130*, 2905–2916. [CrossRef]

39. Galarneau, T.J.; Davis, C.A. Diagnosing Forecast Errors in Tropical Cyclone Motion. *Mon. Weather Rev.* **2013**, *141*, 405–430. [CrossRef]

40. Rogers, R.F.; Reasor, P.; Lorsolo, S. Airborne Doppler observations of the inner-core structural differences between intensifying and steady-state tropical cyclones. *Mon. Weather Rev.* **2013**, *141*, 2970–2991. [CrossRef]

41. Ren, Y.; Zhang, J.A.; Guimond, S.R.; Wang, X. Hurricane Boundary Layer Height Relative to Storm Motion from GPS Dropsonde Composites. *Atmosphere* **2019**, *10*, 339. [CrossRef]

42. Emanuel, K.; Zhang, F. The Role of Inner-Core Moisture in Tropical Cyclone Predictability and Practical Forecast Skill. *J. Atmos. Sci.* **2017**, *74*, 2315–2324. [CrossRef]

43. Blackwell, W.J.; Braun, S.; Bennartz, R.; Velden, C.; DeMaria, M.; Atlas, R.; Dunion, J.; Marks, F.; Rogers, R.; Annane, B.; et al. An overview of the TROPICS NASA Earth Venture Mission. *Q. J. R. Meteorol. Soc.* **2018**, *144*, 16–26. [CrossRef]

44. Ruf, C.; Atlas, R.; Chang, P.S.; Clarizia, M.P.; Garrison, J.L.; Gleason, S.; Katzberg, S.J.; Jelenak, Z.; Johnson, J.T.; Majumdar, S.J.; et al. New ocean winds satellite mission to probe hurricanes and tropical convection. *Bull. Am. Meteorol. Soc.* **2016**, *97*, 385–395. [CrossRef]

45. Lainbrigtsen, B.; Wilson, W.; Tanner, A.; Gaier, T.; Ruf, C.; Piepmeier, J. GeoSTAR—A microwave sounder for geostationary satellites. In Proceedings of the IGARSS 2004. 2004 IEEE International Geoscience and Remote Sensing Symposium, Anchorage, AK, USA, 20–24 September 2004; pp. 777–780.

46. Cotton, J.; Francis, P.; Heming, J.; Forsythe, M.; Reul, N.; Donlon, C. Assimilation of SMOS L-band wind speeds: Impact on Met Office global NWP and tropical cyclone predictions. *Q. J. R. Meteorol. Soc.* **2017**, *144*, 614–629. [CrossRef]

47. Meissner, T.; Ricciardulli, L.; Wentz, F.J. Capability of the SMAP Mission to Measure Ocean Surface Winds in Storms. *Bull. Am. Meteorol. Soc.* **2017**, *98*, 1660–1677. [CrossRef]

48. Chang, Y.; Yang, S.; Lin, K.; Lien, G.; Wu, C. Impact of Tropical Cyclone Initialization on Its Convection Development and Intensity: A Case Study of Typhoon Megi (2010). *J. Atmos. Sci.* **2020**, *77*, 443–464. [CrossRef]

49. Honda, T.; Miyoshi, T.; Lien, G.Y.; Nishizawa, S.; Yoshida, R.; Adachi, S.A.; Terasaki, K.; Okamoto, K.; Tomita, H.; Bessho, K. Assimilating all-sky Himawari-8 satellite infrared radiances: A case of typhoon Soudelor (2015). *Mon. Weather Rev.* **2018**, *146*, 213–229. [CrossRef]

50. Sawada, Y.; Okamoto, K.; Kunii, M.; Miyoshi, T. Assimilating every-10-minute Himawari-8 infrared radiances to improve convective predictability. *J. Geophys. Res. Atmos.* **2019**, *124*, 2546–2561. [CrossRef]

51. Zhang, F.; Minamide, M.; Clothiaux, E.E. Potential impacts of assimilating all-sky infrared satellite radiances from GOES-R on convection-permitting analysis and prediction of tropical cyclones. *Geophys. Res. Lett.* **2016**, *43*, 2954–2963. [CrossRef]

52. Minamide, M.; Zhang, F. An adaptive background error inflation method for assimilating all-sky radiances. *Q. J. R. Meteorol. Soc.* **2019**, *145*, 1–19. [CrossRef]